

# Realization of a three-dimensional photonic topological insulator

Yihao Yang<sup>1,2,3,4</sup>, Zhen Gao<sup>3,4\*</sup>, Haoran Xue<sup>3,4</sup>, Li Zhang<sup>1,2</sup>, Mengjia He<sup>1,2</sup>, Zhaoju Yang<sup>3,4</sup>, Ranjan Singh<sup>3,4</sup>, Yidong Chong<sup>3,4</sup>, Baile Zhang<sup>3,4\*</sup> & Hongsheng Chen<sup>1,2\*</sup>

Confining photons in a finite volume is highly desirable in modern photonic devices, such as waveguides, lasers and cavities. Decades ago, this motivated the study and application of photonic crystals, which have a photonic bandgap that forbids light propagation in all directions<sup>1–3</sup>. Recently, inspired by the discoveries of topological insulators<sup>4,5</sup>, the confinement of photons with topological protection has been demonstrated in two-dimensional (2D) photonic structures known as photonic topological insulators<sup>6–8</sup>, with promising applications in topological lasers<sup>9,10</sup> and robust optical delay lines<sup>11</sup>. However, a fully three-dimensional (3D) topological photonic bandgap has not been achieved. Here we experimentally demonstrate a 3D photonic topological insulator with an extremely wide (more than 25 per cent bandwidth) 3D topological bandgap. The composite material (metallic patterns on

printed circuit boards) consists of split-ring resonators (classical electromagnetic artificial atoms) with strong magneto-electric coupling and behaves like a ‘weak’ topological insulator (that is, with an even number of surface Dirac cones), or a stack of 2D quantum spin Hall insulators. Using direct field measurements, we map out both the gapped bulk band structure and the Dirac-like dispersion of the photonic surface states, and demonstrate robust photonic propagation along a non-planar surface. Our work extends the family of 3D topological insulators from fermions to bosons and paves the way for applications in topological photonic cavities, circuits and lasers in 3D geometries.

Photonic bandgap materials, also known as photonic crystals, are engineered materials that are capable of confining photons because they have photonic bandgaps that forbid the propagation of electromagnetic

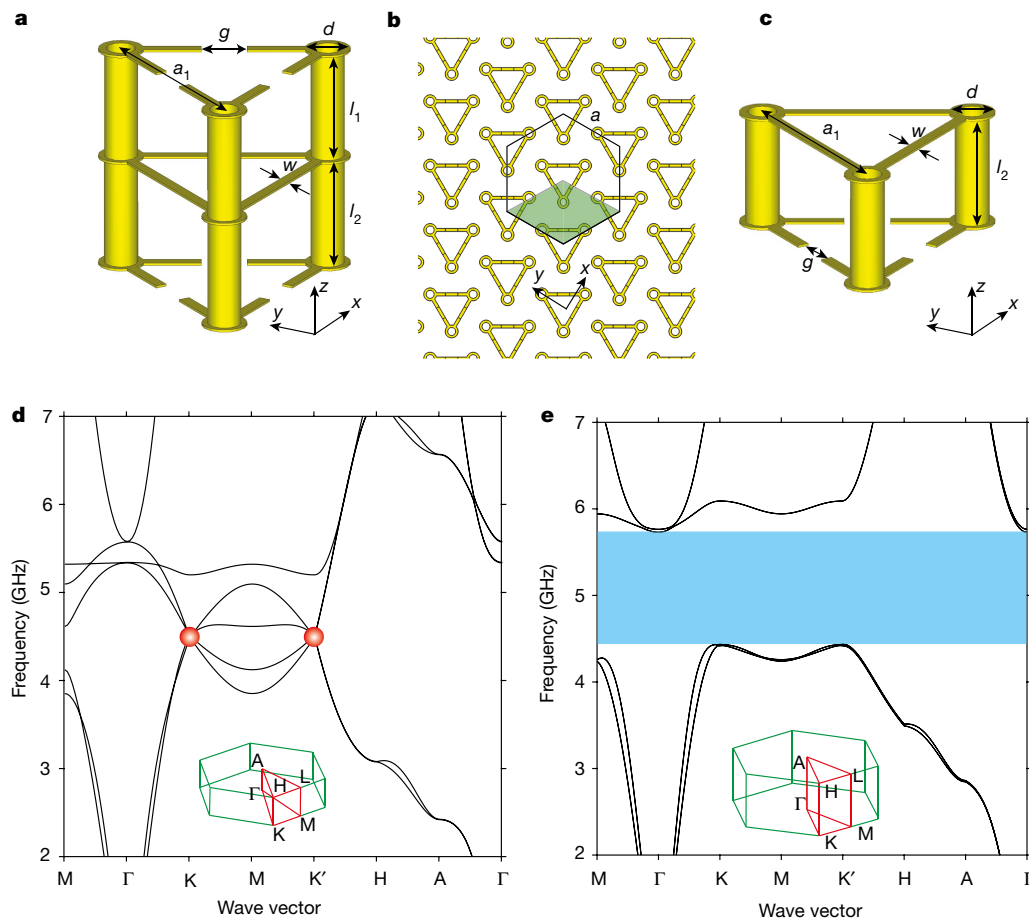


**Fig. 1 | Design of photonic structures with 3D Dirac points and a 3D topological bandgap.** **a, b**, Unit cell (**a**) and top view (**b**) of a hexagonal lattice with 3D Dirac points. The structure parameters are  $l_1 = l_2 = 5$  mm,  $g = 2$  mm,  $a_1 = 9$  mm,  $w = 0.5$  mm,  $d = 1.5$  mm and the lattice constant  $a = 10.4$  mm. The periodicity in the  $z$  direction is 11.3 mm. The background dielectric material has a relative permittivity of 2.5. The green rhombus represents a unit cell. **c**, Unit cell giving rise to a 3D topological bandgap. The top three split-ring resonators (SRRs) in **a** are removed. The three remaining SRRs have the same geometric parameters as in **a**. The periodicity in the  $z$  direction is 5.65 mm. **d, e**, Band diagrams of the crystals with the unit cells shown in **a** and **c**, respectively. Insets show the 3D Brillouin zones for each unit cell. The red dots in **d** are the 3D Dirac points. The blue region in **e** represents the complete topological bandgap.

<sup>1</sup>State Key Laboratory of Modern Optical Instrumentation, The Electromagnetics Academy at Zhejiang University, Zhejiang University, Hangzhou, China. <sup>2</sup>Key Laboratory of Micro-Nano Electronics and Smart System of Zhejiang Province, College of Information Science and Electronic Engineering, Zhejiang University, Hangzhou, China. <sup>3</sup>Division of Physics and Applied Physics, School of Physical and Mathematical Sciences, Nanyang Technological University, Singapore, Singapore. <sup>4</sup>Centre for Disruptive Photonic Technologies, The Photonics Institute, Nanyang Technological University, Singapore, Singapore. \*e-mail: gaozhen@ntu.edu.sg; blzhang@ntu.edu.sg; hansomchen@zju.edu.cn

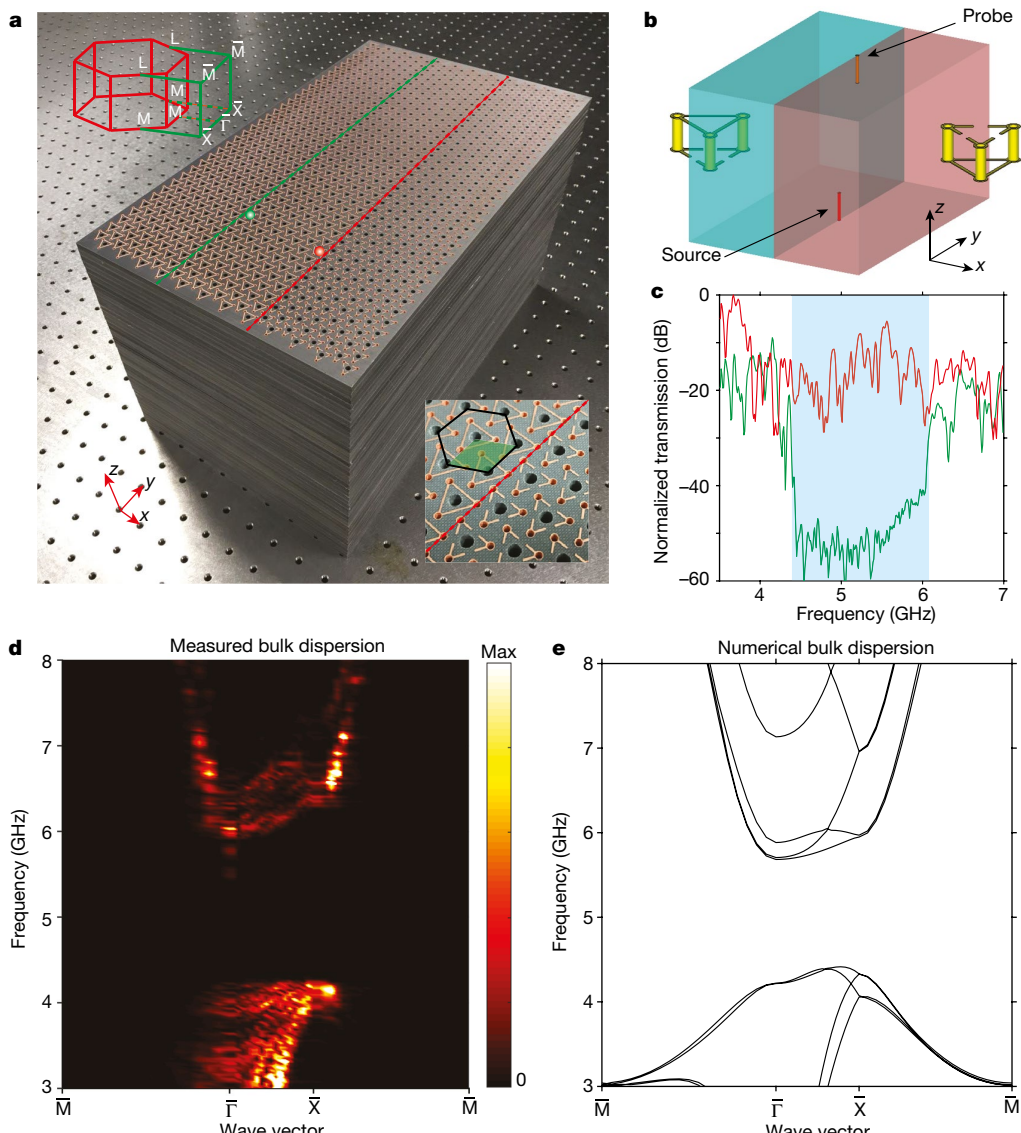


**Fig. 2 | Sample, experimental setup and measured bulk dispersion of the 3D photonic topological insulator.** **a**, Photograph of the sample. The green and red lines indicate the planes used in measuring the bulk and surface states, respectively. The left inset shows the projected Brillouin zone for the domain wall. The right inset is a photograph (with the unit cells marked) near the domain wall. **b**, Experimental setup. The source is positioned at the bottom centre of the surface, while the probe sweeps the

selected plane hole by hole. **c**, Measured surface-state (bulk) transmission at the probe point, located a depth of eight unit cells beneath the red (green) dot. The region highlighted in light blue represents the bulk topological bandgap. **d**, **e**, Measured (**d**) and simulated (**e**) band diagrams of the 3D photonic topological insulator, projected onto the measurement plane. The colour scale in **d** measures the electric energy density  $|E|^2$ .

waves (that is, light waves governed by the classical Maxwell equations) in all directions. Although electronic bandgaps are a long-established concept, it was only in the late 1980s that photonic bandgap materials were theoretically proposed to be an electromagnetic analogue of semiconductor crystals<sup>1,2</sup>. They were then experimentally realized in the form of a 3D photonic crystal with a complete bandgap at microwave frequencies<sup>3</sup>. Researchers have subsequently realized 3D photonic crystals at optical frequencies<sup>12,13</sup>, and shown that photons can be confined in cavities or optical circuits by embedding point, line or volume defects in a 3D photonic crystal<sup>13</sup>. The photon-confining capability of a photonic crystal is generally determined by the width of its bandgap.

Over the past two decades, condensed matter physics has been revolutionized by the introduction of topological classifications of phases of matter, including 2D and 3D topological insulators<sup>4,5</sup>. Whereas 2D topological insulators host topologically protected one-way edge states, 3D topological insulators exhibit topological surface states; these surface states are not unidirectional, but behave as if they were 2D massless Dirac fermions<sup>4,5</sup>. Analogues of 2D topological

insulators, based on numerous different design principles, have been implemented in photonics<sup>14,15</sup>, and can be used to realize topologically protected lasers<sup>9,10</sup> and optical delay lines<sup>11</sup>. However, in these 2D systems, photonic confinement in the third (out-of-plane) direction is achieved by non-topological means such as refractive-index guiding. A 3D topological photonic bandgap, which can achieve topological confinement of photons in all three spatial directions, has not been achieved, to our knowledge. Although topologically non-trivial 3D bandstructures have been demonstrated in Weyl photonic crystals<sup>16–18</sup>, these are ungapped systems (without a bandgap) that cannot be used to confine light.

Recently, there have been several theoretical proposals for realizing a 3D topological photonic bandgap<sup>19–23</sup>. High-index magneto-optic materials can be used to generate a band structure analogous to a ‘strong’ topological insulator (which has an odd number of surface Dirac cones), albeit one with an incomplete bandgap; this has, however, proved challenging to fabricate<sup>20</sup>. Another recent proposal involves a photonic ‘weak’ topological insulator (which has an even number

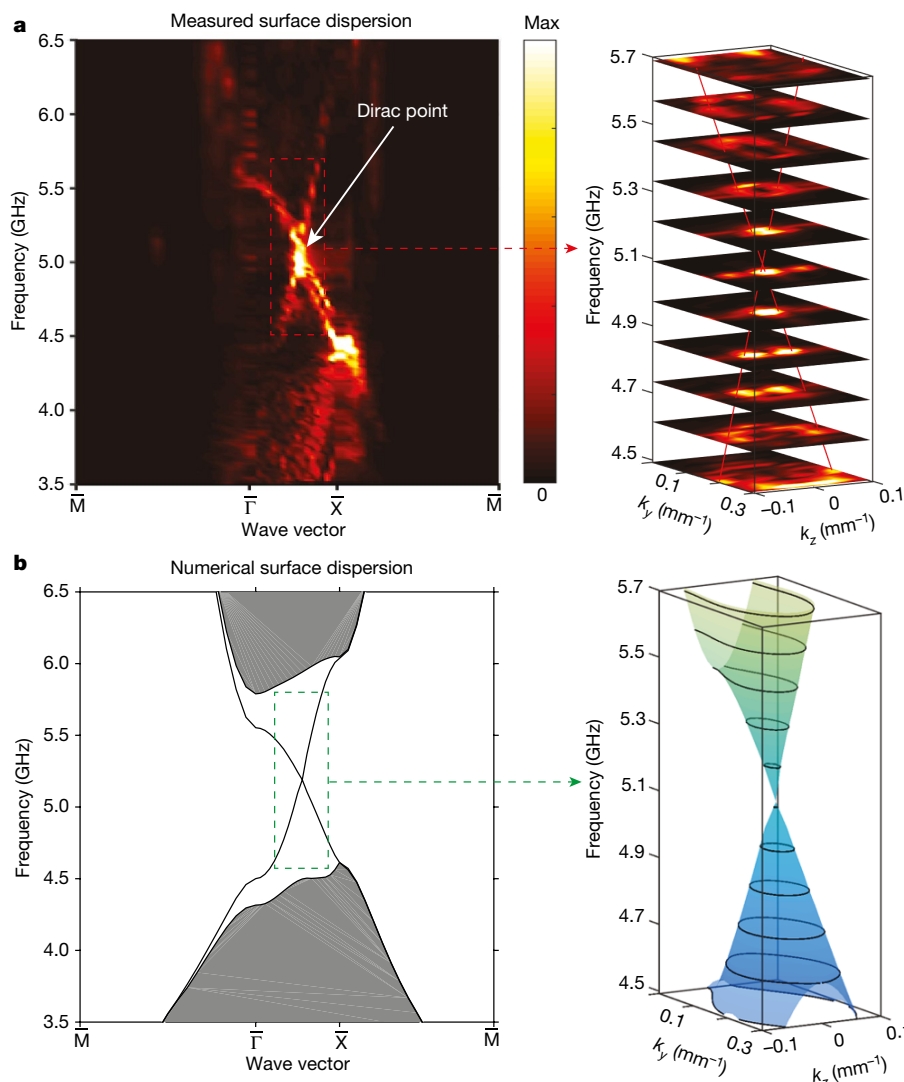


**Fig. 3 | Experimental observation of gapless conical Dirac-like topological surface states of the 3D photonic topological insulator.** **a, b,** Measured (a) and calculated (b) band diagrams for the topological surface states. On the right the isofrequency contours of the topological

surface states at different frequencies are shown. Red lines in a are guides to the eye that indicate the shape of the cones that intersect at the Dirac point. We note that there is another Dirac point near the projection of  $K'$ , not shown here. The colour scale in a measures the electric energy density.

of surface Dirac cones<sup>21</sup>. Weak topological insulators emerge from stacking layers of 2D quantum spin Hall insulators with appropriate interlayer couplings<sup>24</sup>. Although weak-topological-insulator surface states were originally considered to be unprotected against disorder, recent research has revealed that they are robust against disorder, as long as time-reversal symmetry and the existence of the bandgap are maintained<sup>25,26</sup>.

Here we report on the realization of a 3D photonic topological insulator, featuring a complete and extremely wide topological bandgap. We have experimentally mapped out the bulk bandstructure and the dispersion of the surface states along an internal domain wall. We show explicitly that the surface states have the predicted form of a Dirac cone<sup>21</sup>, which is the key distinguishing feature of a 3D photonic topological insulator. We also experimentally demonstrate robust photonic transport in 3D along a sharply twisted internal domain wall. Unlike the proposal of Slobozhanyuk et al.<sup>21</sup>, our design utilizes a 3D array of metallic split-ring resonators (SRRs), which are classical electromagnetic artificial atoms that serve as building blocks for metamaterials<sup>27</sup>. The resonance-enhanced bi-anisotropy of the SRRs has a role analogous to that of strong spin-orbit coupling in topological insulator materials<sup>4,5</sup>, allowing for a topological bandgap with width greater than 25%. This exceeds previously demonstrated topological bandgap widths even in 2D, which have been 10% or less<sup>7,9–11,14,28,29</sup>, and substantially exceeds

the gap widths in previous 3D proposals, which were of the order of a few per cent or incomplete<sup>19–23</sup>.

We start with a photonic crystal design featuring an ungapped bandstructure with 3D Dirac points. As depicted in Fig. 1a, the photonic crystal has a unit cell consisting of six connected metallic SRRs. The crystal is formed by arranging the unit cells in a triangular lattice in the  $x$ - $y$  plane, as shown in Fig. 1b, and stacking identical layers along the  $z$  direction. The background material is Teflon woven glass fabric copper-clad laminate, with a relative permittivity of 2.5. Note that the back-to-back arrangement of the SRRs cancels the bi-anisotropy at the  $K$  and  $K'$  points in the Brillouin zone<sup>30</sup>. The lattice has a mirror ( $z \rightarrow -z$ ) symmetry, which we denote  $\sigma_z$ . For fine-tuned lattice parameters, the photonic bandstructure exhibits frequency-isolated 3D Dirac points<sup>21</sup> (that is, doubly degenerate Weyl points), with four-fold degeneracy at the band-crossing points at  $K$  and  $K'$ , as shown in Fig. 1d.

The design for a wide-gap photonic topological insulator is shown in Fig. 1c. These SRRs are not arranged back-to-back and so  $\sigma_z$  is broken. This unit cell can be formed by removing the upper three SRRs in the unit cell of Fig. 1a and adjusting the  $z$  periodicity accordingly. The resulting bandstructure is shown in Fig. 1e, and exhibits a wide ( $>25\%$ ) bandgap. Although the relationship between the two photonic crystal designs is not immediately apparent, we show in Methods that the bandgap in Fig. 1e is continuously deformable into the infinitesimal

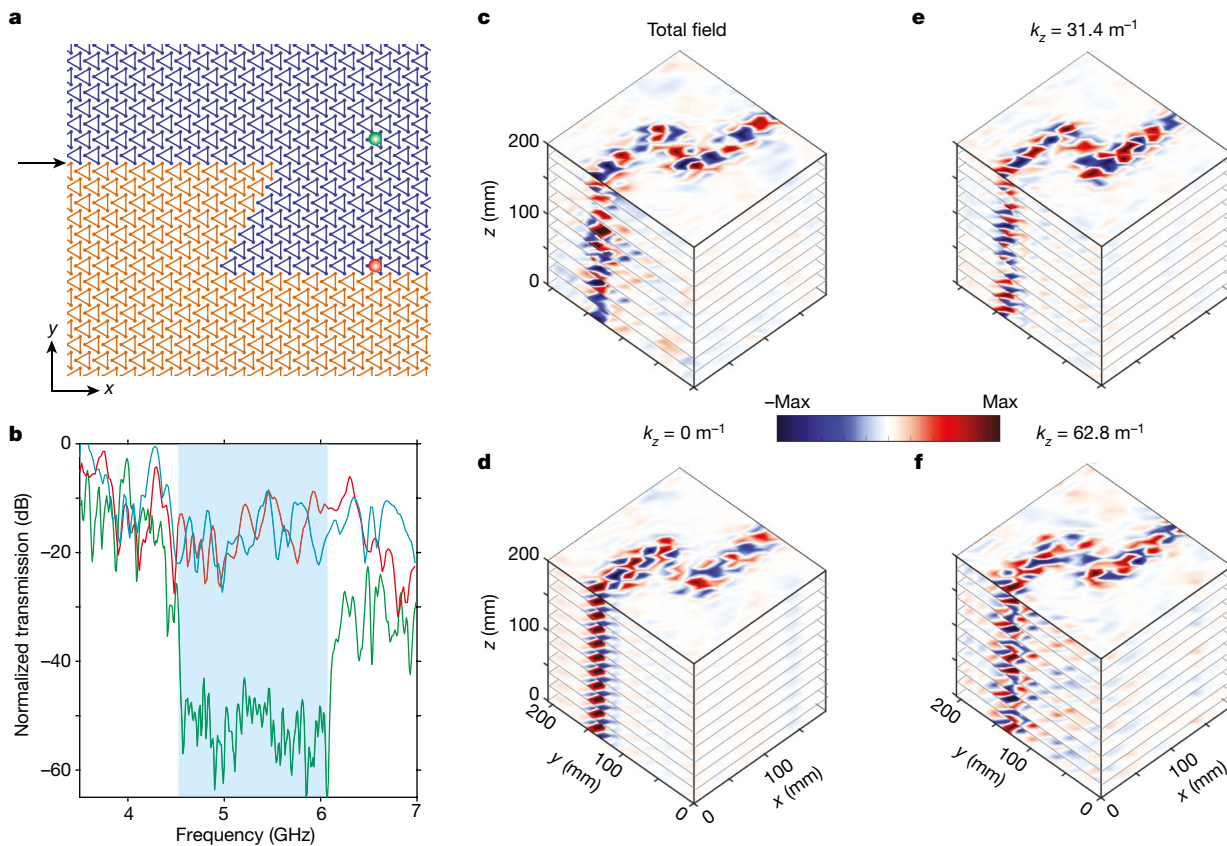


**Fig. 4 | Experimental demonstration of the robustness of photonic topological surface states.** **a**, Cross-sectional schematic of the fabricated sharply twisted domain wall. The orange (blue) triangles in the upper (lower) domain represent the unit cells of SRRs with downward (upward) openings. A point-like source is located at the  $x$ - $y$  position indicated by the black arrow, with the  $z$  position in the middle of the sample. The red (green) dot indicates the  $x$ - $y$  position of the detector used to

measure the surface-state transmission (bulk transmission). **b**, Measured transmission for surface states along the twisted/straight domain wall (red/blue line) and for bulk states (green line). The region highlighted in light blue represents the bulk topological bandgap. **c**, Measured total field distribution in the  $x$ - $y$  plane for different  $z$ , at 4.7 GHz. **d–f**, Measured field distributions in the  $x$ - $y$  plane with different  $z$  and different values of  $k_z$ , at 4.7 GHz.

bandgap opened at the Dirac points when the  $\sigma_z$  symmetry of Fig. 1a is perturbatively broken. In the original  $\sigma_z$ -symmetric structure, the electric and magnetic dipoles have opposite parity and form decoupled modes under in-plane propagation ( $k_z = 0$ ). Breaking  $\sigma_z$  induces a bi-anisotropic coupling between the in-plane electric and magnetic dipoles, generating two hybrid modes in each of the lower and upper bands. Near the K and K' valleys, the pair of eigenmodes within each band have electric and magnetic components that are respectively in-phase or out-of-phase, corresponding to pseudospin-up or pseudospin-down, for both lower and upper bands<sup>15,21,29,31</sup>. This form of bi-anisotropic coupling has previously been shown to have a role analogous to that of Kane–Mele spin–orbit coupling in quantum spin Hall materials<sup>4,5,15,21,31</sup>. See Methods for theoretical characterization of the topological properties.

The experimental sample of a photonic topological insulator is shown in Fig. 2a (see Methods). In the first set of experiments, illustrated in Fig. 2b, a dipole source antenna is inserted from the bottom centre of the  $y$ - $z$  plane, indicated by the red (green) dotted line in Fig. 2a, four unit cells into the bulk; a second dipole antenna, acting as the probe, is inserted inside the sample from the hole marked with a red (green) dot in Fig. 2a, at a depth of eight unit cells into the bulk, to measure the transmission of the surface (bulk) states. We wrapped all sides of the sample with microwave absorbers. The frequency dependence of the transmittance, along the domain wall, and in the bulk, is shown in Fig. 2c. We observe an approximately 20-dB drop in the transmittance of the bulk states, extending from approximately 4.3 GHz to 6.0 GHz, corresponding to a bulk bandgap. Along the domain wall, however, the transmittance remains high throughout the frequency range, indicating the existence of surface states. Numerical simulations reveal

that pseudospin–momentum locking occurs along the isofrequency contours of the surface Dirac cone, which is another key feature of 3D photonic topological insulators<sup>21,31</sup> (see Methods).

To probe the bulk bandstructure, we measure the electromagnetic response in the  $y$ - $z$  plane (indicated by the green dotted line in Fig. 2a) away from the domain wall. The probe dipole antenna is fixed to a robotic arm, and we map the complex electric field patterns in the selected plane. After Fourier transformation to reciprocal space, we obtain the plot shown in Fig. 2d, which closely matches the numerically computed projected bandstructure shown in Fig. 2e. We note that there is a complete photonic bandgap in the bulk, with almost the same frequency range as the bandgap in Fig. 2c.

Next, we repeat the field measurements with the source and probe located along the 2D domain wall. The surface bandstructure, shown in Fig. 3a, reveals a family of surface states that span the frequency range of the bulk bandgap, forming a conical dispersion curve. The surface Dirac point occurs at 5.1 GHz, near the mid-point of the bulk bandgap, and along the  $\Gamma$ -X high-symmetry line (near the projection of the K point of the 3D Brillouin zone). A second Dirac point near K' is not shown in this plot. The isofrequency plots in the 2D reciprocal space confirm that the dispersion is indeed conical, as shown on the right in Fig. 3a. These results closely match the numerically computed surface bandstructure, as shown in Fig. 3b. By placing the probes in adjacent unit cells, away from the domain wall, we verify that the surface states are tightly confined to the domain wall with a penetration depth of around 10.3 mm (see Methods).

Finally, we demonstrate robust propagation of the surface states along a non-planar domain wall. As schematically shown in Fig. 4a, the wall is sharply twisted, with two 60° corners. A waveguide (marked

by a black arrow) launches topological surface states that propagate to the right. The measured transmission along the twisted domain wall (at the position of the red dot) is comparable to that measured along the previous straight domain wall of the same length, as shown in Fig. 4b. In comparison, the measured transmission in the bulk (at the green dot in Fig. 4a) is substantially lower, owing to the bulk bandgap. We also performed a 3D map of the field distributions at 4.7 GHz (see Methods). The results, shown in Fig. 4c, demonstrate that the topological surface states flow robustly along the surface, including around the two sharp corners. Extracting different  $k_z$  components, we plot in Fig. 4d–f the field distributions with  $k_z = 0 \text{ m}^{-1}$ ,  $k_z = 31.4 \text{ m}^{-1}$  and  $k_z = 62.8 \text{ m}^{-1}$ , respectively. (These are typical values in the range of the allowable  $k_z$ ; see Methods.) Negative values of  $k_z$  behave similarly and are therefore omitted. The results match well with the numerical results (see Methods).

Our work thus demonstrates a classical photonic analogue of a 3D topological insulator. The realization of a 3D topological photonic bandgap opens the door to a wide range of topological photonic devices, such as topological photonic lasers<sup>9,10</sup> and circuits in previously inaccessible 3D geometries. This also provides the opportunity to study topological quantum optics beyond 2D<sup>28</sup>, such as spontaneous emission<sup>1</sup> in a fully 3D topological cavity. Although our demonstration was carried out at microwave frequencies, the design principles should be generalizable to other frequency regimes. Current advances in 3D SRR fabrication have shown that operating frequencies at terahertz and infrared frequencies are feasible<sup>32</sup>. An implementation based on all-dielectric metamaterials<sup>21</sup> may allow for a 3D photonic topological insulator in the optical regime. We focused here on a photonic crystal for electromagnetic waves, but a similar lattice design may be applied to other bosonic systems, such as acoustic and mechanical structures<sup>33</sup>.

## Online content

Any methods, additional references, Nature Research reporting summaries, source data, statements of data availability and associated accession codes are available at <https://doi.org/10.1038/s41586-018-0829-0>.

Received: 15 April; Accepted: 25 October 2018;

Published online 9 January 2019.

- Yablonovitch, E. Inhibited spontaneous emission in solid-state physics and electronics. *Phys. Rev. Lett.* **58**, 2059–2062 (1987).
- John, S. Strong localization of photons in certain disordered dielectric superlattices. *Phys. Rev. Lett.* **58**, 2486–2489 (1987).
- Yablonovitch, E., Gmitter, T. & Leung, K. Photonic band structure: the face-centered-cubic case employing nonspherical atoms. *Phys. Rev. Lett.* **67**, 2295–2298 (1991).
- Hasan, M. Z. & Kane, C. L. Topological insulators. *Rev. Mod. Phys.* **82**, 3045–3067 (2010).
- Qi, X.-L. & Zhang, S.-C. Topological insulators and superconductors. *Rev. Mod. Phys.* **83**, 1057–1110 (2011).
- Lu, L., Joannopoulos, J. D. & Soljačić, M. Topological photonics. *Nat. Photon.* **8**, 821–829 (2014).
- Khanikaev, A. B. & Shvets, G. Two-dimensional topological photonics. *Nat. Photon.* **11**, 763–773 (2017).
- Ozawa, T. et al. Topological photonics. Preprint at <https://arxiv.org/abs/1802.04173> (2018).
- Bahari, B. et al. Nonreciprocal lasing in topological cavities of arbitrary geometries. *Science* **358**, 636–640 (2017).
- Bandres, M. A. et al. Topological insulator laser: experiments. *Science* **359**, eaar4005 (2018).
- Hafezi, M., Demler, E. A., Lukin, M. D. & Taylor, J. M. Robust optical delay lines with topological protection. *Nat. Phys.* **7**, 907–912 (2011).
- Lin, S.-y. et al. A three-dimensional photonic crystal operating at infrared wavelengths. *Nature* **394**, 251–253 (1998).
- Rinne, S. A., García-Santamaría, F. & Braun, P. V. Embedded cavities and waveguides in three-dimensional silicon photonic crystals. *Nat. Photon.* **2**, 52–56 (2008).
- Wang, Z., Chong, Y., Joannopoulos, J. D. & Soljačić, M. Observation of unidirectional backscattering-immune topological electromagnetic states. *Nature* **461**, 772–775 (2009).

- Khanikaev, A. B. et al. Photonic topological insulators. *Nat. Mater.* **12**, 233–239 (2013).
- Lu, L. et al. Experimental observation of Weyl points. *Science* **349**, 622–624 (2015).
- Noh, J. et al. Experimental observation of optical Weyl points and Fermi arc-like surface states. *Nat. Phys.* **13**, 611–617 (2017).
- Yang, B. et al. Ideal Weyl points and helicoid surface states in artificial photonic crystal structures. *Science* **359**, 1013–1016 (2018).
- Yannopapas, V. Gapless surface states in a lattice of coupled cavities: a photonic analog of topological crystalline insulators. *Phys. Rev. B* **84**, 195126 (2011).
- Lu, L. et al. Symmetry-protected topological photonic crystal in three dimensions. *Nat. Phys.* **12**, 337–340 (2016).
- Slobobchuk, A. et al. Three-dimensional all-dielectric photonic topological insulator. *Nat. Photon.* **11**, 130–136 (2017).
- Lin, Q., Sun, X.-Q., Xiao, M., Zhang, S.-C. & Fan, S. Constructing three-dimensional photonic topological insulator using two-dimensional ring resonator lattice with a synthetic frequency dimension. Preprint at <https://arxiv.org/abs/1802.02597> (2018).
- Ochiai, T. Gapless surface states originating from accidentally degenerate quadratic band touching in a three-dimensional tetragonal photonic crystal. *Phys. Rev. A* **96**, 043842 (2017).
- Fu, L., Kane, C. L. & Mele, E. J. Topological insulators in three dimensions. *Phys. Rev. Lett.* **98**, 106803 (2007).
- Mong, R. S., Bardarson, J. H. & Moore, J. E. Quantum transport and two-parameter scaling at the surface of a weak topological insulator. *Phys. Rev. Lett.* **108**, 076804 (2012).
- Ringel, Z., Kraus, Y. E. & Stern, A. Strong side of weak topological insulators. *Phys. Rev. B* **86**, 045102 (2012).
- Pendry, J. B., Holden, A. J., Robbins, D. & Stewart, W. Magnetism from conductors and enhanced nonlinear phenomena. *IEEE Trans. Microw. Theory Tech.* **47**, 2075–2084 (1999).
- Barik, S. et al. A topological quantum optics interface. *Science* **359**, 666–668 (2018).
- Cheng, X. et al. Robust reconfigurable electromagnetic pathways within a photonic topological insulator. *Nat. Mater.* **15**, 542–548 (2016).
- Marqués, R., Medina, F. & Rafii-El-Idrissi, R. Role of bianisotropy in negative permeability and left-handed metamaterials. *Phys. Rev. B* **65**, 144440 (2002).
- Ma, T., Khanikaev, A. B., Mousavi, S. H. & Shvets, G. Guiding electromagnetic waves around sharp corners: topologically protected photonic transport in metawaveguides. *Phys. Rev. Lett.* **114**, 127401 (2015).
- Burckel, D. B. et al. Micrometer-scale cubic unit cell 3D metamaterial layers. *Adv. Mater.* **22**, 5053–5057 (2010).
- Süsstrunk, R. & Huber, S. D. Observation of phononic helical edge states in a mechanical topological insulator. *Science* **349**, 47–50 (2015).

**Acknowledgements** We thank Q. Yan at Zhejiang University, L. Lu at the Chinese Academy of Sciences and J. C. W. Song at Nanyang Technological University for discussions. The work at Zhejiang University was sponsored by the National Natural Science Foundation of China under grant numbers 61265502, 61574127, 61601408, 61775193 and 11704332, the ZJNSF under grant number LY17F010008, the Top-Notch Young Talents Program of China, the Fundamental Research Funds for the Central Universities and the Innovation Joint Research Center for Cyber-Physical-Society System. Y.C. and B.Z. acknowledge the support of Singapore Ministry of Education under grant numbers MOE2015-T2-1-070, MOE2015-T2-2-008, MOE2016-T3-1-006 and Tier 1 RG174/16 (S). Y.Y. and R.S. acknowledge the support of the Singapore Ministry of Education under grant number MOE2015-T2-2-103.

**Reviewer information** *Nature* thanks J. Bravo-Abad and the other anonymous reviewer(s) for their contribution to the peer review of this work.

**Author contributions** Y.Y. initiated the original idea. Y.Y., B.Z. and H.C. designed the experiment. Y.Y., Z.G., M.H. and L.Z. fabricated samples. Y.Y. and Z.G. carried out the measurement and analysed data. Y.Y., H.X., L.Z. and Z.Y. performed simulations. Y.Y., H.X., B.Z., M.H., Z.Y., H.C. and Y.C. provided the theoretical explanations. R.S. assisted in part of the experiment. Y.Y., Y.C., B.Z. and H.C. supervised the project.

**Competing interests** The authors declare no competing interests.

## Additional information

**Extended data** is available for this paper at <https://doi.org/10.1038/s41586-018-0829-0>.

**Supplementary information** is available for this paper at <https://doi.org/10.1038/s41586-018-0829-0>.

**Reprints and permissions information** is available at <http://www.nature.com/reprints>.

**Correspondence and requests for materials** should be addressed to Z.G. or B.Z. or H.C.

**Publisher's note:** Springer Nature remains neutral with regard to jurisdictional claims in published maps and institutional affiliations.

## METHODS

**Design procedure: from 3D Dirac points to a wide 3D topological bandgap.** The 3D topological bandgap is designed by finding a structure with 3D Dirac points, and then lifting the degeneracy. Consider a 3D Dirac metamaterial that exhibits 3D Dirac points at K and K' in the Brillouin zone (Extended Data Fig. 1a). We then slightly reduce the heights of the upper SRRs ( $l_1$ ), as well as the thicknesses of the spacers ( $t_{\text{top}}$ ) above the upper SRRs. This perturbation breaks the  $\sigma_z$  inversion symmetry and induces magneto-electric coupling in the unit cells. The magneto-electric coupling has a role similar to that of spin-orbit coupling in condensed matter systems<sup>15,21,29,31</sup>, and results in the opening of a small topologically complete bandgap at the 3D Dirac point<sup>21,34</sup>, as shown in Extended Data Fig. 1b.

Next, with the ratio of  $t_{\text{top}}/l_1$  unchanged, the top SRRs are continuously compressed. The width of the bandgap monotonously increases and reaches a maximum when the top SRRs completely disappear (Extended Data Fig. 1c–g). The first bandgaps (marked in blue) in Extended Data Fig. 1b–g are topologically equivalent, because they are never closed throughout this process.

**Modes near the K and K' valleys.** There are four degenerate modes at each Dirac point, corresponding to the four bands labelled 1 to 4 in Extended Data Fig. 1a. Extended Data Fig. 2a plots the current distributions of different modes in the unit cell near the K valley. Two of the modes are of transverse-electric polarization, with even and odd (the red dashed line denotes the mirror plane) current distributions (labelled  $e_+$  and  $e_-$ ); the other two modes are of transverse-magnetic polarization, with even and odd current distributions (labelled  $m_+$  and  $m_-$ ). Extended Data Fig. 2b (corresponding to the situation in Extended Data Fig. 1b) shows that the  $\sigma_z$  symmetry breaking induces a bi-anisotropic coupling between transverse-magnetic and transverse-electric polarizations, giving rise to  $e_{\pm} \pm m_{\mp}$  modes in the upper bands, and  $e_{\pm} \mp m_{\mp}$  modes in the lower bands. As shown in the second and third rows of Extended Data Fig. 2b, in these modes, the electric and magnetic components are either in-phase or out-of-phase, corresponding to the photonic pseudospin-up or pseudospin-down states as defined in the previous literature<sup>29,31</sup>. These pseudospin states are connected through a time-reversal symmetry operation<sup>15,31</sup>; in the first band, the pseudospin-up near the K valley transforms to the pseudospin-down near the K' valley, and vice versa. In the lower-band modes, the surface current is mainly localized at the bottom of the SRRs. Therefore, as the heights of the upper SRRs are continuously reduced, the lower-band modes (including their pseudospins) almost remain unchanged (Extended Data Fig. 2c, corresponding to the situation in Extended Data Fig. 1g).

**Effective Hamiltonian at the K (K') valley of the 3D photonic topological insulator.** Following refs<sup>21,31</sup> closely, we obtain the effective Hamiltonian near the K (K') valley of the 3D photonic topological insulator with  $k$ -theory:

$$H = \omega_D \Delta_0 + v_D (\delta k_x \sigma_x + \delta k_y \sigma_y) + v_{\perp} \delta k_z \sigma_y + m_r s_z \sigma_z$$

where  $s_i$  and  $\sigma_i$  ( $i = x, y, z$ ) are Pauli matrices,  $v_D$  is the in-plane group velocity at the 3D Dirac point,  $v_{\perp}$  is the out-of-plane group velocity,  $\omega_D$  is the degeneracy frequency of the 3D Dirac point,  $\Delta_0$  causes an overall blueshift of the bands, and  $m_r$  is the effective mass term induced by the bi-anisotropy. See Supplementary Information for detailed derivation and the Berry curvature calculation.

**Domain wall and spin-momentum locking of topological surface states.** A schematic view of the domain wall is shown in Extended Data Fig. 3a. The blue and red regions contain down-oriented and up-oriented SRRs, respectively. In Extended Data Fig. 3b, the spin-momentum locking of the topological surface states on the isofrequency contour at 4.8 GHz is simulated. The black (red) arrows in the right panel indicate the magnetic (electric) fields inside the cross-sections of the SRRs near the domain wall. When encircling the isofrequency contour, the polarization of the surface states evolves from left-handed circular polarization to linear polarization, right-handed circular polarization, linear polarization, and finally left-handed circular polarization. This is also associated with changes of the phase difference between the electric and magnetic dipole components, which varies from 0 to  $2\pi$  along the contour. These results are consistent with

those in ref.<sup>21</sup>. See Supplementary Information for the analytical derivation of spin-momentum locking.

The topological states in our case are protected by electromagnetic duality, tied to the design of the unit cell<sup>21</sup>. Thus, unlike other crystalline topological insulator designs<sup>35,36</sup>, the boundary of this 3D photonic topological insulator does not break topological protection, and the surface Dirac cones are gapless<sup>21</sup>.

**Simulated field distributions near a sharply twisted 2D domain wall.** Extended Data Fig. 4a shows the simulated robust energy transport of the topological surface states along a sharply twisted 2D domain wall. The schematic view of the domain wall is shown in Extended Data Fig. 4a, where the green and red triangles represent the down-oriented and up-oriented SRRs, respectively. A dipole source is placed at the left end of the domain wall to excite the surface states in the simulation. The out-of-plane boundary condition is set to be periodic boundaries with  $k_z$  indicated in each subfigure, and the in-plane boundaries are open. The distributions of the electric field intensity across the domain wall at different  $k_z$  clearly show robust energy transport.

**Experimental samples.** The sample is fabricated with printed circuit board technology by etching 5-mm-thick dielectric laminates with double-sided, 0.035-mm-thick copper cladding. Each printed layer is paired with a 0.65-mm-thick dielectric spacer. At the centre of each unit cell is an air hole of radius 1.5 mm, which allows an electromagnetic probe to be inserted to measure the fields within the crystal. The sample consists of 40 identical layers, stacked along the  $z$  axis, with a domain wall separating the two domains with opposite  $\sigma_z$ -breaking (that is, the SRRs in the two domains are oriented upside-down relative to each other), as shown in Fig. 2a, b. The domain wall thus lies in the  $y$ - $z$  plane (marked by a red dotted line in Fig. 2a), with size  $45 \times 40$  unit cells.

**Measurements.** The field spectra are measured with a vector network analyser (R&S ZVL13). Complex field patterns are obtained by measuring the field distributions point-by-point with the aid of a 3D movement platform (Linbou NFS03). Extended Data Fig. 5a shows the measured electric field distributions (including both phase and amplitude) in the sample of the straight domain wall. In Extended Data Fig. 5b, the green dots show the measured energy density (proportional to the square of the field intensity) summed along the  $z$  direction, as a function of the distance from the domain wall. The green dashed line is numerically fitted to an exponential function  $\exp(-|y|/d)$ , where  $y$  is the coordinate. The fitted penetration depth is  $d \approx 10.3$  mm, comparable to the unit cell size. These results show that the surface states are strongly confined to the domain wall (denoted by the black dashed line in Extended Data Fig. 5a). The dispersion in Extended Data Fig. 5c is obtained by applying a Fourier transform to the complex field pattern in real space at the domain wall. See Supplementary Information for more details.

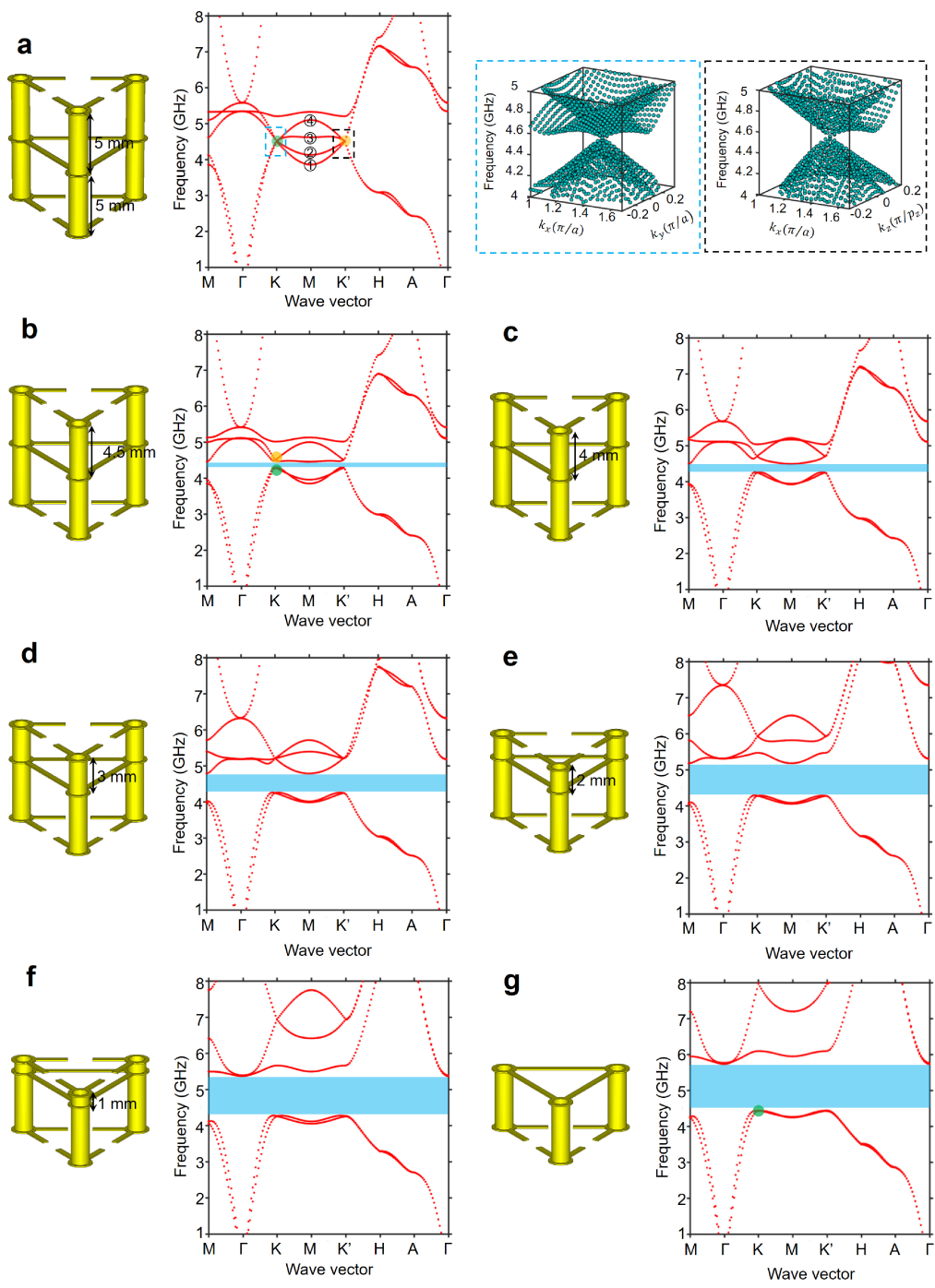
**Numerical simulations.** The band diagrams of the 3D Dirac metamaterial and the 3D photonic topological insulator are numerically simulated with a finite-element method solver (COMSOL Multiphysics RF Module). The simulations of 3D photonic topological insulator surface states are performed in the eigenvalue module of CST Microwave Studio. In these simulations, a vertical domain wall in the middle of a supercell consisting of 16 unit cells is considered. For bulk (surface) band structure calculations, periodic boundary conditions are imposed on all surfaces of the unit cell (supercell) to form an infinite hexagonal (rectangular) lattice.

**Code availability.** The codes used to create the plots in this paper are available from DR-NTU Institutional Repository: <https://doi.org/10.21979/N9/29T8VJ>.

## Data availability

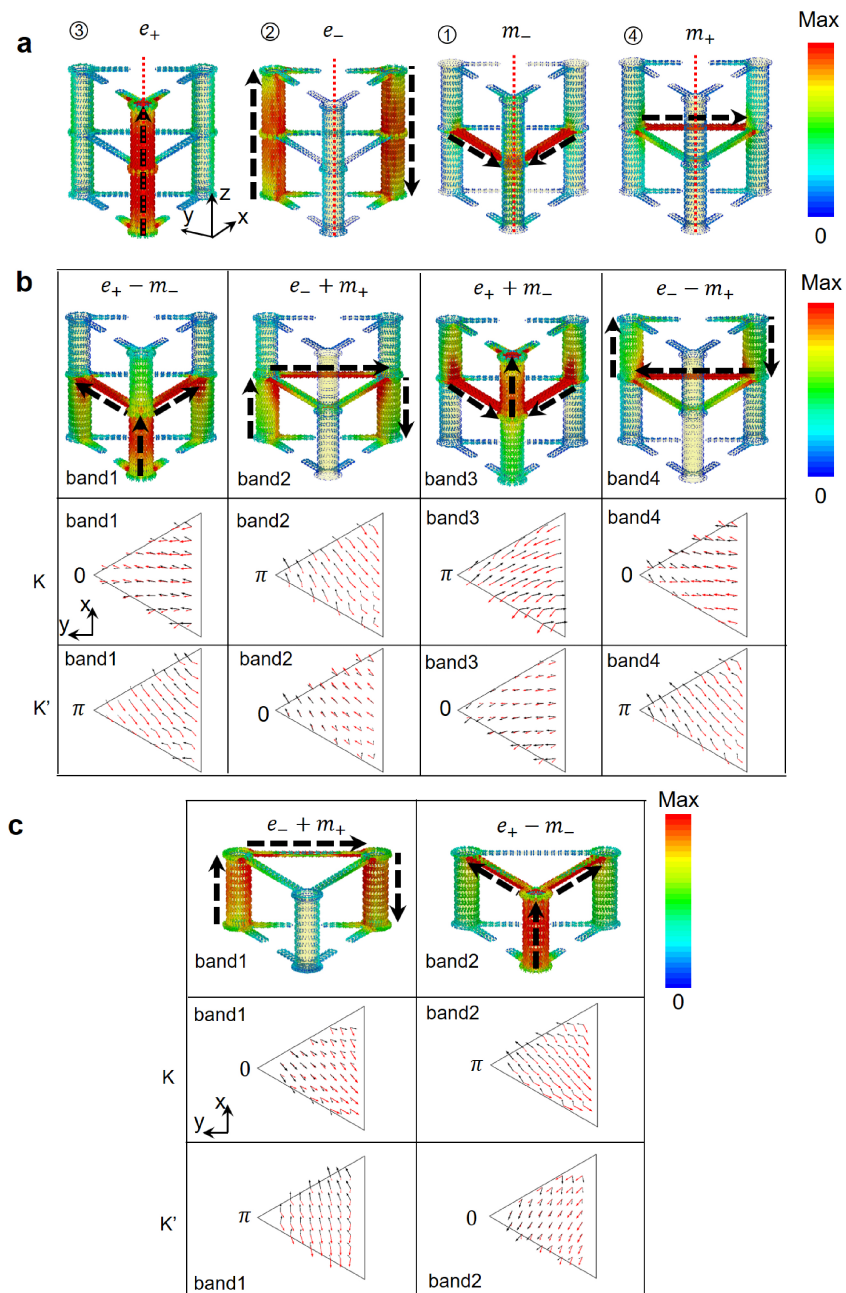
The data that support the findings of this study are available from the corresponding authors on reasonable request.

- 34. Guo, Q. et al. Three dimensional photonic Dirac points in metamaterials. *Phys. Rev. Lett.* **119**, 213901 (2017).
- 35. Wu, L.-H. & Hu, X. Scheme for achieving a topological photonic crystal by using dielectric material. *Phys. Rev. Lett.* **114**, 223901 (2015).
- 36. Yves, S. et al. Crystalline metamaterials for topological properties at subwavelength scales. *Nat. Commun.* **8**, 16023 (2017).



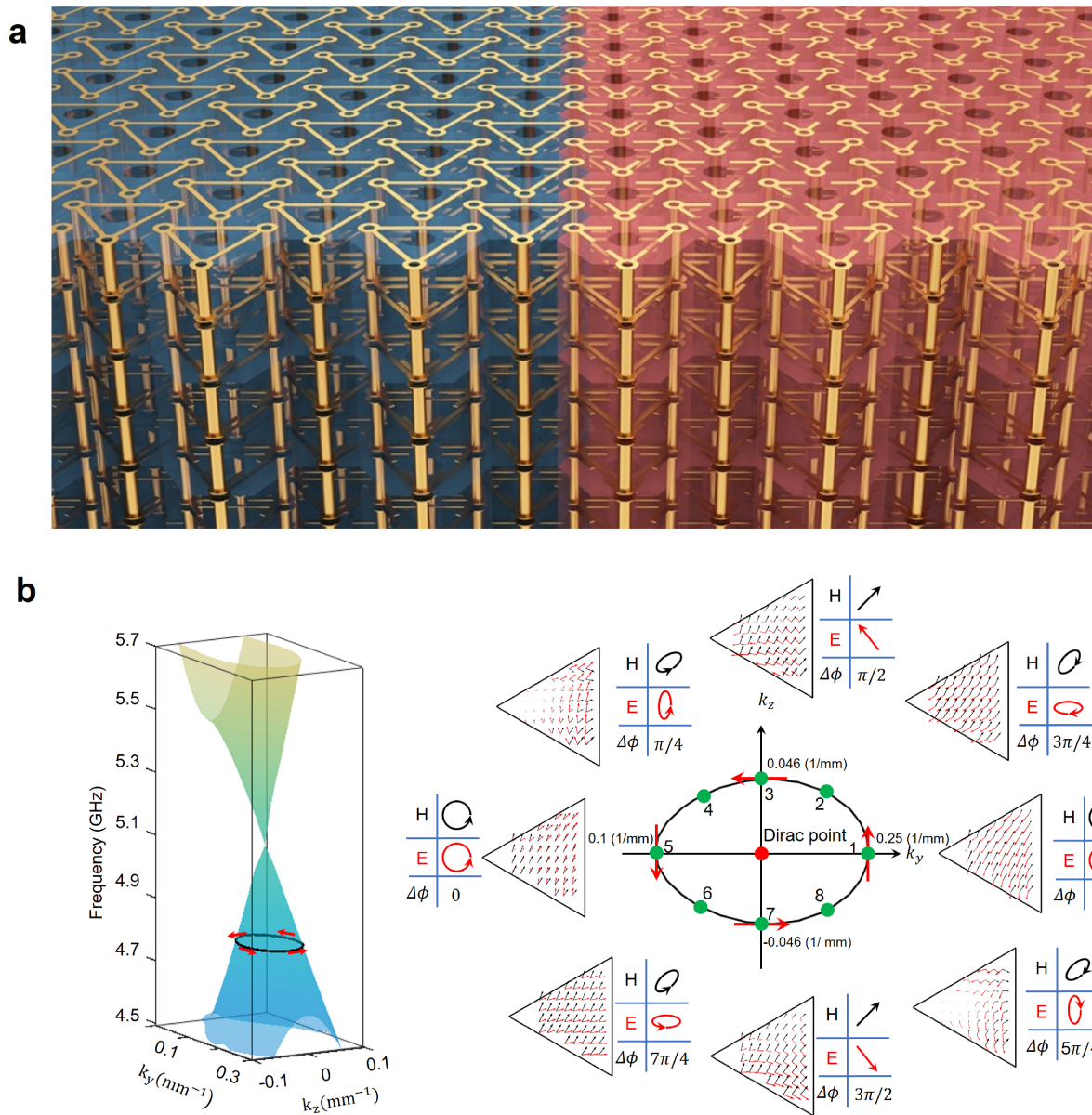
**Extended Data Fig. 1 | Bandstructure evolutions.** **a**, Hexagonal unit cell and band diagram of the 3D photonic crystal. The green and yellow dots indicate the 3D Dirac points. The plots on the right show the 2D projection of the 3D Dirac cones in the vicinity of the K and K' points.

**b-g**, Hexagonal unit cell and bandstructures for different  $l_1$ . Here,  $a$  is the lattice constant in the  $x$ - $y$  plane and  $p_z$  is the periodicity in the  $z$  direction; the ratio of  $t_{\text{top}}$  to  $l_1$  remains unchanged, while  $l_1$  is gradually compressed to zero. The blue regions represent the first (primary) bandgaps.



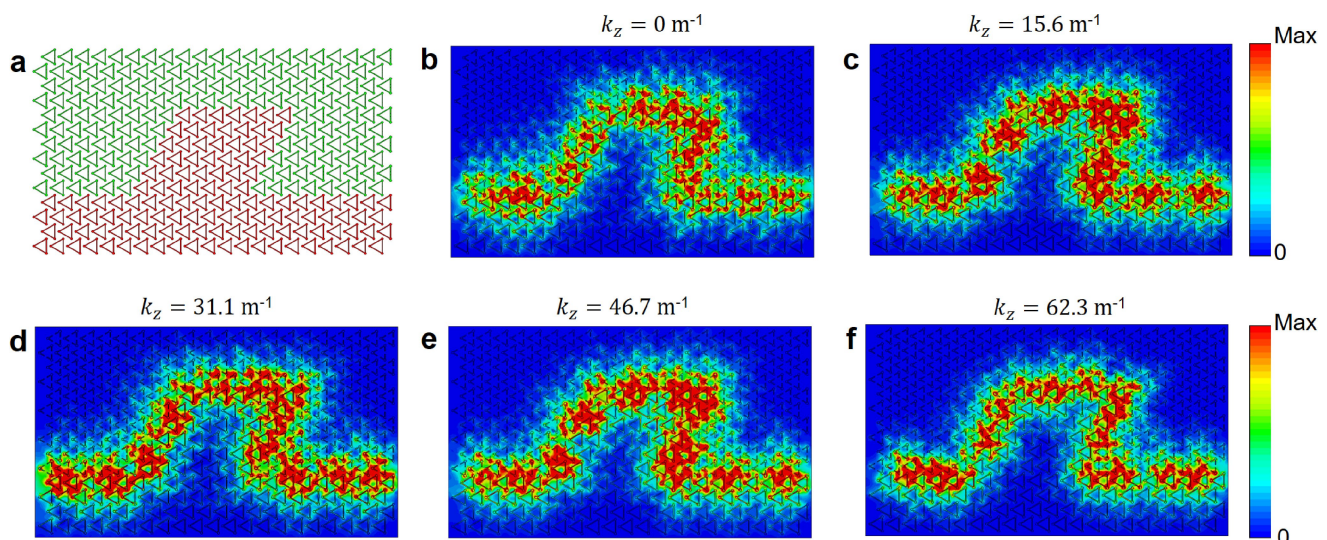
**Extended Data Fig. 2 | Modal analysis.** **a**, Modal analysis for 3D Dirac points. Current distributions of four degenerate modes near the 3D Dirac point marked by the green dot in Extended Data Fig. 1a. The dashed arrows represent the current directions, and  $e_+$  ( $e_-$ ) and  $m_+$  ( $m_-$ ) represent the even (odd) transverse-electric and transverse-magnetic modes, respectively. Here, the even and odd modes are classified by the mirror plane indicated by the red dotted lines. **b**, Modal analysis for the 3D photonic topological insulator with a small perturbation. The first row shows the current distributions of the hybrid modes at the lower bands (green dot in Extended Data Fig. 1b) and upper bands (yellow dot in Extended Data Fig. 1b) near the K valley. The dashed arrows represent the current directions. The previous four degenerate modes hybridize pairwise

and split into the lower and upper bands, respectively. The second and third rows show the cross-sectional polarization configurations of electric (red) and magnetic (black) fields, near the K and K' valleys. The phase difference between electric and magnetic dipole components is 0 or  $\pi$ . **c**, Modal analysis for the wide-gap 3D photonic topological insulator. The first row shows the current distributions of the lower-band modes (green dot in Extended Data Fig. 1g) near the K valley. The dashed arrows represent the current directions. The second and third rows show the cross-sectional polarization configurations of electric (red) and magnetic (black) fields, near the K and K' valleys. The phase difference between electric and magnetic dipole components is 0 or  $\pi$ .



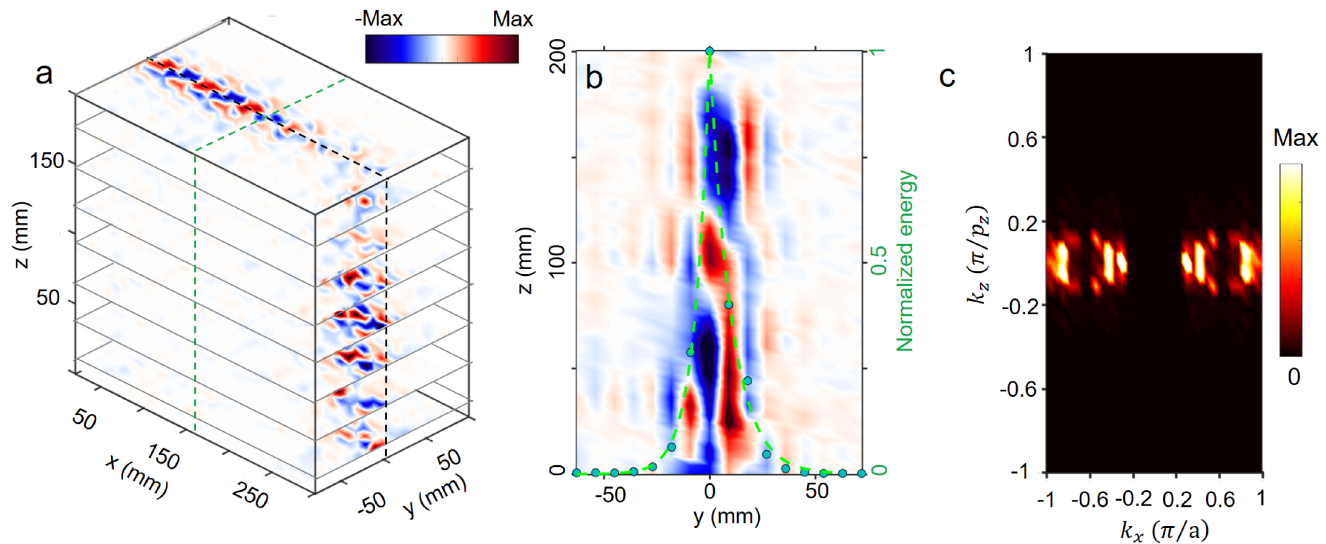
**Extended Data Fig. 3 | Spin–momentum locking of topological surface states.** **a**, Schematic of the domain wall. The openings of the SRRs in the left and right of the domains are opposite. **b**, Spin–momentum locking at an isofrequency (4.8-GHz) contour of the surface Dirac cone. On the left is a dispersion diagram of the surface Dirac cone. The black ring indicates the isofrequency contour and the red arrows illustrate the spin–momentum locking at 4.8 GHz. On the right are schematic and numerical

results of the polarization configurations of electric (red) and magnetic (black) fields inside the cross-sections of the SRRs (triangles), at eight points marked on the isofrequency contour by green dots and numbers. The phase difference between the electric and magnetic components,  $\Delta\phi$ , varies from 0 to  $2\pi$  along the contour. The black ring and red dot represent the isofrequency contour and surface Dirac point, respectively.



**Extended Data Fig. 4 | Simulated field distributions near a sharply twisted 2D domain wall.** a, Schematic of the twisted domain wall: the red and green triangles are SRRs oriented upwards and downwards,

respectively. b–f, Distributions of the electric field intensity across the domain wall, with different values of  $k_z$ .



**Extended Data Fig. 5 | Measured field distributions and the corresponding dispersion.** **a**, Measured electric field distributions in the sample of a straight domain wall in the  $x$ - $y$  plane at different heights of  $z$  at 4.7 GHz. The black dashed line represents the position of the domain wall; the green dashed line denotes the position of the cross-section shown in **b**.

**b**, Field distributions and normalized electric energy density in the  $y$ - $z$  plane with  $x = 150$  mm. The dots and dashed line represent experimental data and exponential fitting, respectively. **c**, Surface dispersion in momentum space, obtained by Fourier transforming the real-space complex field distributions on the domain wall.